

Ion acceleration in shell cylinders irradiated by a short intense laser pulse

A. Andreev,^{1,2} K. Platonov,³ A. Sharma,² and M. Murakami⁴

¹Max-Born Institute, Berlin, Germany

²ELI-ALPS, Szeged, Hungary

³St. Petersburg State Polytechnic University, St. Petersburg, Russia

⁴ILE, Osaka University, Osaka, Japan

(Received 29 April 2015; accepted 11 August 2015; published online 4 September 2015)

The interaction of a short high intensity laser pulse with homo and heterogeneous shell cylinders has been analyzed using particle-in-cell simulations and analytical modeling. We show that the shell cylinder is proficient of accelerating and focusing ions in a narrow region. In the case of shell cylinder, the ion energy exceeds the ion energy for a flat target of the same thickness. The constructed model enables the evaluation of the ion energy and the number of ions in the focusing region. © 2015 AIP Publishing LLC. [<http://dx.doi.org/10.1063/1.4929850>]

INTRODUCTION

Ion acceleration driven by ultraintense, ultrashort laser pulses has been intensively studied in the past decade due to the number expected future applications. However, the production of high-quality ion beams is still being researched (see, for example, Ref. 1). Nanostructured targets (NST), in particularly carbon nano-tubes,² have extraordinary material and mechanical properties. An ion acceleration schemes using NSTs, working at extreme conditions has been previously proposed^{3–5} and in this paper, NSTs are irradiated by an ultrashort intense laser to generate quasi-monoenergetic collimated ion beams. Typically, a NST is irradiated by a 10–20 fs pulse (laser intensity $> 10^{18}$ Wcm²). The duration of the ultrashort pulse corresponds to the characteristic time of a Coulomb explosion⁶ which in the order of the ion plasma wave period. Under such conditions, low-Z materials, like hydrogen, are fully ionized, while materials such as carbon are substantially ionized and electrons are ejected by the laser pulse within a few periods.

ANALYTICAL MODEL OF LIGHT ION ACCELERATION IN A TARGET WITH HEAVY IONS

The interaction of short intense laser pulse with a target of shell cylinder shape, which consists of ions of two sorts, is considered. A very high contrast pulse is used because the laser pulse shape is very important for a mass limited target.⁹ As the laser pulse duration is shorter than the characteristic acceleration ion time, the acceleration process occurs after the pulse termination when hot electrons completely fill the limited target. During the acceleration, the laser target expands and the electron gas in the target obey the adiabatic law, $p_e/n_e^\gamma = T_{e0}/n_{e0}^{\gamma-1}$ where p_e and n_e are the pressure and concentration of hot electrons, respectively, and T_{e0} and n_{e0} are the initial values of their temperature and concentration. Because the acceleration time of ions is longer than the time of the motion of a relativistic electron through the limited target, the inertia of electron can be neglected in the hydrodynamic equation of motion. Thus, the condition of local equilibrium of the electron gas in a cylinder target can be

stated as $e\partial\varphi/\partial r = -n_e^{-1}\partial p_e/\partial r$, where φ is the scalar potential of the ambipolar field in the target and e is the electron charge. Using the adiabatic law of expansion of the electron gas, the electron concentration can be expressed from the balance equation of forces in terms of the potentials

$$n_e(\varphi) = n_{e0} \left(1 + \frac{\gamma - 1}{\gamma} \frac{e\varphi}{T_{e0}} \right)^{\frac{1}{\gamma-1}}.$$

The chosen adiabatic index is $\gamma = 2$, which is compatible with 2D geometry. Therefore, the two dimensional Poisson equation for determining the potential and the field that accelerates ions becomes linear $\Delta\varphi = -4\pi e [Zn_{1i}(r) + n_{2i} - n_e(\varphi)]$ and can be solved for a cylinder target.

The density of the positive heavy ion charge for limited cylinder shell target can be written as $n_{1i}(r, z) = n_{1i0}\theta(r - r_1)\theta(r_2 - r) \cdot \theta(H - |z|)$, where $r_{1,2}$ are the inner and outer radii of the shell, $2H$ is cylinder height and $\theta(z)$, $\theta(r)$ are the step functions. The density of light ions is taken as ultra thin layer (contamination thickness ~ 10 nm, $s_2 \ll r_1$) at the inner surface of cylinder: $n_{2i}(r) = n_{2i0}s_2\delta(r - r_1) \cdot \theta(H - |z|)$. The acceleration of light ions from the outer surface is not considered.

The system is normalized with the coordinates normalize to the inner shell radius: $\xi = r/r_1$, $\varsigma = z/r_1$; time to the ion plasma frequency $\tau = \omega_{pi}t$, $\omega_{pi}^2 = 4\pi Z^2 n_{1i0}e^2/m_i$ and the introduction of the dimensionless potential $\psi = |e|\varphi/T_{e0}$. In dimensionless variables, the Poisson equation for the dimensionless concentration of hot electrons, which is linearly related with the potential $\psi = 2(\eta_e - 1)$, takes the following form:

$$2\rho^2 \left(\frac{\partial^2}{\partial \xi^2} + \frac{1}{\xi} \frac{\partial}{\partial \xi} + \frac{\partial^2}{\partial \varsigma^2} \right) \eta_e = \eta_0 \eta_e - \theta(\xi - \xi_1)\theta(\xi_2 - \xi) \cdot \theta(h - |\varsigma|) - \varepsilon \delta(\xi - \xi_1) \cdot \theta(h - |\varsigma|), \quad (1)$$

where $r_D^2 = T_{e0}/4\pi e^2 Z n_{1i0}$, $\eta_0 = n_{e0}/Z n_{1i0}$, $\rho = r_D/r_1$, $h = H/r_1$, $\varepsilon = n_{2i0}s_2/Z n_{1i0}r_1 \ll 1$, and the equation of proton motion can be written in the following form:

$$\frac{\partial^2 \zeta}{\partial \tau^2} = -\frac{2\rho^2}{\eta_0} \frac{\partial \eta_e}{\partial \zeta}, \quad \frac{\partial^2 \xi}{\partial \tau^2} = -\frac{2\rho^2}{\eta_0} \frac{\partial \eta_e}{\partial \xi}. \quad (2)$$

Eqs. (1) and (2) describe the acceleration of light ions by heavy shell cylinder heated by short laser pulse. The density of the heavy ions n_{i0} in (1) only reaches solid density value by the removal of all electrons from cylinder walls (high temperature limit). At the partial removal of the electrons, the quasi-neutrality ratio: $2\pi Z n_{i0} r_1 (r_2 - r_1) \approx 2\pi n_{e0} r_1 2r_{De}$,

$r_{De}^2 = T_{e0}/4\pi e^2 Z n_{e0}$ connects the densities of particles and temperature, thus the cylinder potential is determined by the temperature and density of hot electrons. The parameters T_{e0} and n_{e0} are the initial conditions in the considered in the acceleration model. Its values are calculated using particle-in-cell (PIC) simulations and, where appropriate, analytical estimations. A thin cylinder is when $\Delta r = r_2 - r_1 \ll r_1$ and the influence of light ions on heavy ones is negligible ($\varepsilon \rightarrow 0$). The solution of Eq. (1) in this scenario can be written as

$$\eta_e(\xi, \varsigma) = \begin{cases} \int_0^\infty dk \frac{2\xi_1(\xi_2 - \xi_1) \cos k\varsigma \sin kh}{\pi k \sqrt{2\rho^2 k^2 + \eta_0}} I_0\left(\xi \sqrt{k^2 + \eta_0/2\rho^2}\right) K_0\left(\xi_1 \sqrt{k^2 + \eta_0/2\rho^2}\right), & \xi < \xi_1 \\ \int_0^\infty dk \frac{2\xi_1(\xi_2 - \xi_1) \cos k\varsigma \sin kh}{\pi k \sqrt{2\rho^2 k^2 + \eta_0}} K_0\left(\xi \sqrt{k^2 + \eta_0/2\rho^2}\right) I_0\left(\xi_1 \sqrt{k^2 + \eta_0/2\rho^2}\right), & \xi > \xi_1, \end{cases} \quad (3)$$

where $\xi_1 = 1$. Due to complexity of the integral, it is simpler to analyze Eq. (3) in the case of a large and small (when compared to the Debye radii) cylinder radius r_1 . In the limit of a large cylinder radius, $\rho \ll \sqrt{\eta_0}$, Eq. (1) shows that the electron and ion density are very similar. Considering the asymptotic nature of the modified Bessel functions at big argument, the electron density can be obtained from Eq. (3) (when $h \gg 1$)

$$\eta_e(\xi, \varsigma) \approx \theta(|h| - \varsigma) (\xi_2 - \xi_1) \sqrt{\eta_0/8\rho^2} \times \exp(-|\xi - \xi_1| \sqrt{\eta_0/2\rho^2}). \quad (4)$$

The potential obtained from Eq. (4) looks like radial potential well where test particles undergo radial oscillations. The electric field component along cylinder axis at $h \gg 1$ is very weak at the cylinder edges thus such limit is not optimal for particle acceleration along this axis. For a cylinder of small radius $\rho \gg \sqrt{\eta_0}$, Eq. (3) can be simplified to

$$\begin{aligned} \varphi(z, r) &= 4\sigma r_1 \int_0^{\pi/2} d\phi \\ &\times \ln \left[\frac{z + h + \sqrt{(z + h)^2 + (r - r_1)^2 + 4rr_1 \sin^2 \phi}}{z - h + \sqrt{(z - h)^2 + (r - r_1)^2 + 4rr_1 \sin^2 \phi}} \right], \\ \sigma &= Z e n_{i0} (r_2 - r_1). \end{aligned} \quad (5)$$

This potential in Eq. (5) is shown in Fig. 1, using the values $\sigma = 1$, $\xi_1 = 1$, $h = 2$ as an example. In the limit of $z \rightarrow \infty$, Eq. (5) reduces to a point charge form where $\varphi \rightarrow 4\pi\sigma r_1 H/|z|$. If the length of the cylinder $H = 0$, the resultant potential at $z = 0$ plane is given by $\varphi(r, 0) = 4\sigma r_1^2 |r_1 - r|^{-1} F[-4rr_1/(r_1 - r)]$ where the function F denotes the complete elliptic integral of the first kind. For the domain $r_1 < r \ll r_D$, the potential approaches $\varphi \rightarrow 2\pi\sigma r_1^2/r$.

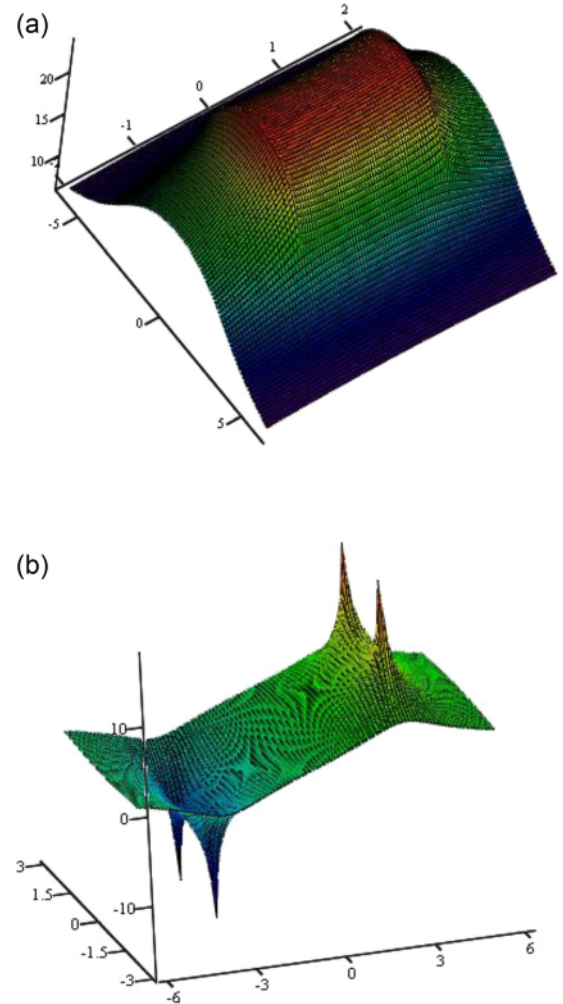


FIG. 1. (a) Three-dimensional view of the potential (5) at $\sigma = 1$, $\xi_1 = 1$, and $h = 2$; (b) The surface of E_z —electric field z -component at $(r_2 - r_1)/r_1 = 1/15$.

Inside the cylinder, the electrostatic field has a saddle structure and the potential surface is convex along the z -axis and concave along the r -axis. As a result of the saddle shape potential, the interior ions are compressed around the z -axis then accelerated along the axis, toward both ends of the cylinder. Eq. (1) can be used to estimate the proton energy at the edge of the cylinder as $\varepsilon_p \approx e\varphi_m$, where

$$\begin{aligned}\varphi_m &= \varphi(z=H, r=0) \approx 2\pi r_1 \sigma \ln[2h + \sqrt{4h^2 + 1}] \\ &\approx \frac{Zen_{i0}V}{2H} \ln(4h), \\ V &= 2\pi r_1 \Delta r 2H,\end{aligned}$$

$\varepsilon_p \approx e\varphi_m \approx \frac{T_e 2\pi Z e^2 n_{i0} r_1 \Delta r}{T_e} \ln(4h) = T_e \frac{r_1 \Delta r}{2r_D^2} \ln(4\frac{H}{r_1})$, here $\sigma = Q_m/S = Zen_{i0}S\Delta r/S = Zen_{i0}\Delta r$.

For the conditions $r_1 = 1 \mu\text{m}$, $\Delta r = 0.1 \mu\text{m}$, $n_{i0} = 6 \cdot 10^{22} \text{cm}^{-3}$, $H = 1.5 \mu\text{m}$, there is proton energy of $\varepsilon_p \sim 30 \text{MeV}$.

In the case of low potential wall (Fig. 2(a)), the protons, which are located at the shell, slide to the cylinder axis and does not oscillate as in the case of a deep potential wall.

The numerical solution of ion equation of motion (Eq. (2)) in the potential (Eq. (5)) is shown in Fig. 3.

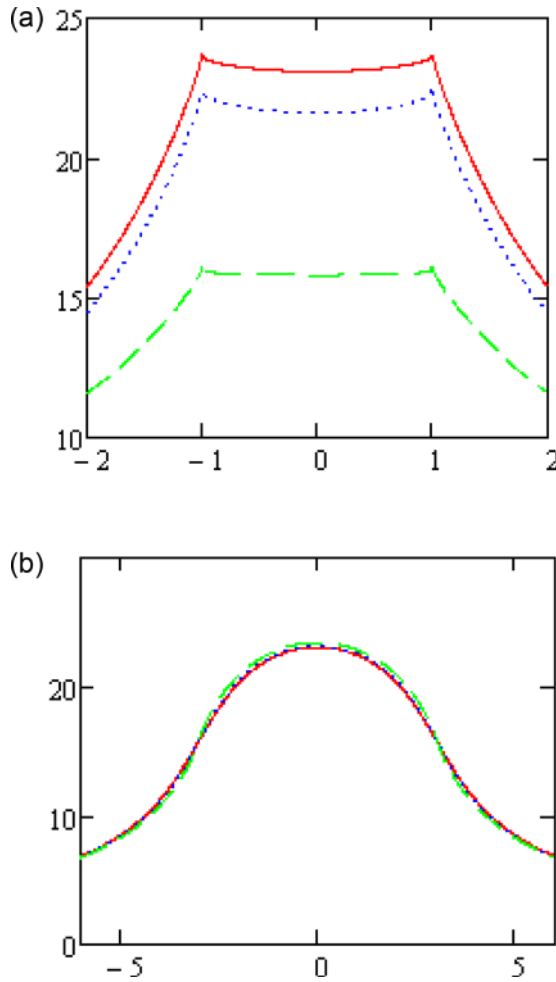


FIG. 2. (a) Radial cross sections of the normalized cylinder potential (5) where red solid line is $\psi(0, \xi)$, blue dotted line is $\psi(0.5h, \xi)$, green dashed line is $\psi(h, \xi)$. (b) Axial cross sections of the potential where red solid line is $\psi(\xi, 0)$, blue dotted line is $\psi(\xi, 0.5)$, green dashed line is $\psi(\xi, 0.9)$. Here $\sigma = 1$, $\xi_1 = 1$, $h = 3$.

Proton trajectory is determined by its initial position (ξ_0, ς_0) in the thin inner cylinder surface layer. Thus, protons have almost the same ξ_0 at the starting time $t=0$. Fig. 3(a) shows that the light ions propagate with a good collimation along the z -axis and by comparison of red and blue trajectories, it can be concluded that proton angle has a slight dependence on ς_0 in the interval $0.01h \leq \varsigma_0 \leq 0.7h$. Only ions located near the cylinder edge, $\varsigma_0 \sim h$, have a significant deviation from the cylinder axis. The dependence of proton propagation angle χ (with respect to cylinder axis) upon its initial coordinate, ς_0 , is shown in Fig. 3(b) for cylinders of different relative lengths. The proton collimation arises from the relatively small radial potential wall in comparison with the cylinder axis “hump” (Fig. 2). A good measure of the collimation is the ratio $v_r/v_z = \tan \chi$, where $v_{z,r}$ denote the average velocities of the light ions in the axial and radial directions at big ($\varsigma \geq 3h$) distance from the cylinder. In Fig. 3, the angle of proton trajectory (in degree) was calculated by Eq. (2) at the point $\varsigma = 3h$, where proton trajectory was already in straight line. The following formula can be used for estimating the average

$$\begin{aligned}\text{proton angle: } \frac{v_r}{v_z} &\approx \sqrt{\frac{\varphi'_r}{\varphi'_z}} \approx \sqrt{\left(\frac{r-r_1}{S_- - S_+}\right) \left(\frac{S_-}{z+h+S_+} - \frac{S_+}{z-h+S_-}\right)}, \\ \text{where } S_{\pm} &= \sqrt{(z \pm h)^2 + (r - r_1)^2}.\end{aligned}$$

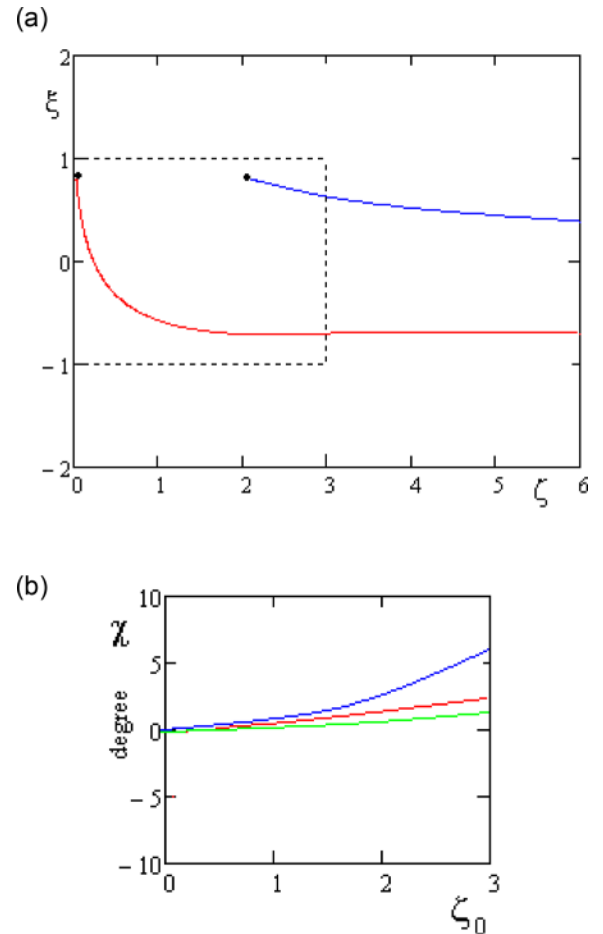
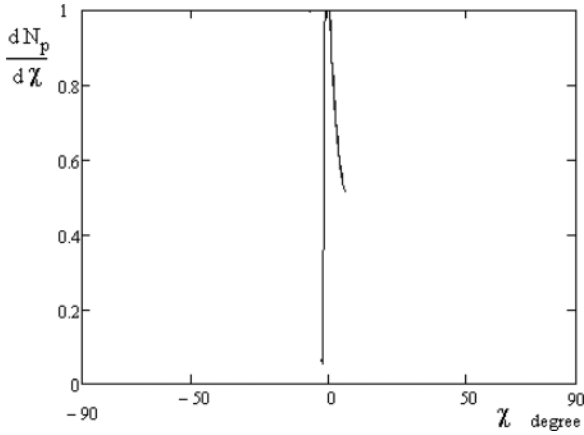


FIG. 3. (a) The proton trajectories with different initial position $\xi_0 = 0.01h$, $0.7h$, and $\xi_0 = 0.9\xi_1$ in the potential (5); (b) the dependence of the proton propagation angle χ on its axial initial coordinates ξ_0 at $\xi_0 = 0.9$, $\sigma = 1$, $\xi_1 = 1$, and $h = 3$ —red line, $h = 2$ —blue line, $h = 4$ —green line.

FIG. 4. The angular proton distribution function at $\sigma = 1$, $\xi_1 = 1$, $h = 2$.

This estimation is in agreement with Fig. 3(b) when using the initial proton coordinates as $r = r_0$, $z = z_0$.

The number of protons accelerated inside cylinder from the surface of initial radius r_0 and located in the interval dz_0 is $dN_p = 2\pi r_0 n_{2i0} s_2 dz_0$. Dividing this number with the angular interval $d\chi$ gives $dN_p/d\chi$, and thus a parametric dependent (parameter z_0) proton angular distribution function can be written

$$\frac{dN_p}{d\chi} = 2\pi n_{2i0} s_2 r_0 \left/ \left| \frac{d\chi(z_0)}{dz_0} \right| \right., \quad \chi = \chi(z_0), \quad z_0 \in [0; H]. \quad (6)$$

Eq. (6) shows that the maximum angular distribution occurs at $d\chi(z_0)/dz_0 \approx 0$ and hence there is the maximum at around the zero angle (Fig. 4).

The number of protons accelerated inside cylinder from the surface of radius r_0 is $dN_p = 2\pi r_0 n_{2i0} s_2 dz_0$. The proton energy is determined by the potential at its position $\varepsilon_p(z_0) = e\varphi(z_0, r_0)$, and therefore the proton energy distribution is determined by the parametric dependence

$$\frac{dN_i}{d\varepsilon_i} = 2\pi r_0 n_{2i0} s_2 \frac{dz_0}{e d\varphi(z_0, r_0)} = \frac{2\pi r_0 n_{2i0} s_2}{e |E_z(z_0, r_0)|}, \quad (7)$$

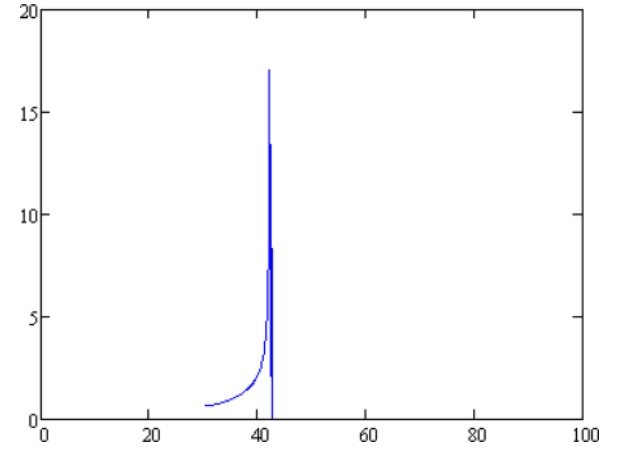
$$\varepsilon_i(z_0) = e\varphi(z_0, r_0), \quad z_0 \in [0; H].$$

The field $E_z(r, z_0 = 0) = 0$ and there is also the potential maximum at $z = 0$, thus the distribution function is greatest at the maximal proton energy. At $z_0 \neq 0$, the distribution function (Eq. (7)) is limited and located in the energetic interval according to the ordinates of the green curve in Fig. 2(b), at $-h < \varsigma_0 < h$.

The proton energy distribution has a narrow peak with a sharp cut-off. Increasing the cylinder height make potential profile flatter (Fig. 2(b)), and produces a narrowing of energy distribution (Fig. 5). A longer cylinder increases time of proton flight at the same energy.

OPTIMAL TARGET PARAMETERS FOR MAXIMAL PROTON ACCELERATION ALONG CYLINDER AXIS

Within this regime, $r_1 \leq r_D$ and it is clear there is almost no electric field components within the cylinder as $h \rightarrow \infty$.

FIG. 5. The proton energy distribution function at $\sigma = 1$, $\xi_1 = 1$, $h = 2$.

Thus, the resultant acceleration lasts for a long time and heavy ions will expand before protons receive a significant energy. In the case when $h \rightarrow 0$, protons are not axial focused and expand isotropy. This model is limited and no optimal h value could be found.

The model is modified by assuming that the total charge of cylinder ions is constant $N = 2\pi r_1 \Delta r Z n_{1i0} 2H \approx \text{const}$. The characteristic target ions velocity is $c_s \approx \sqrt{Z T_e / m_i}$ and time $t_{pi} \approx \omega_{pi}^{-1}$ results in a distance $c_s t_{pi} \approx r_D$ travelled. Thus, the cylinder length cannot be less than r_D , and $4\pi r_1 \Delta r \cdot n_{1i0} \approx N / (H + H_0)$, where $H_0 \sim r_D$. The energy of proton with initial coordinates (r_0, z_0) can be written as

$$\varepsilon_p(z_0, r_0; H, r_1) = \frac{Ze^2 N}{\pi(H + H_0)} \int_0^{\pi/2} d\theta \times \ln \left[\frac{z_0 + H + \sqrt{(z_0 + H)^2 + (r_0 - r_1)^2 + 4r_0 r_1 \sin^2 \theta}}{z_0 - H + \sqrt{(z_0 - H)^2 + (r_0 - r_1)^2 + 4r_0 r_1 \sin^2 \theta}} \right]. \quad (8)$$

Fig. 2(b) shows that proton energy weakly depends on r_0 and the maximal proton energy from Eq. (8) can be calculated using

$$\varepsilon_{pm} \approx \varepsilon_p(0, 0, H, r_1) \approx 2\pi Ze^2 n_{1i0} r_1 (r_2 - r_1) \ln \left[\frac{\sqrt{H^2 + r_1^2} + H}{\sqrt{H^2 + r_1^2} - H} \right]. \quad (9)$$

The case of almost full removal of electrons from a gold cylinder (with a fraction of carbon and hydrogen) has been considered⁴ where $H = 15$ nm, $r_2 = 7.5$ nm, and $r_2 - r_1 \approx 3$ nm. The maximum proton energy calculated from this model (at $\rho \gg \sqrt{\eta_0}$) for these parameters is shown in Fig. 6 and has the same 1.5 MeV value reported in Ref. 4. Fig. 6 shows that the optimal ratio $h = 2.5$ is located between two vertical dashed lines, again similar to the reported result in Ref. 4. If electrons are partially removed then $2\pi Ze^2 n_{1i0} r_1 \Delta r = Ze^2 N / (H + H_0) \approx T_e$ and quasi-neutrality is assumed

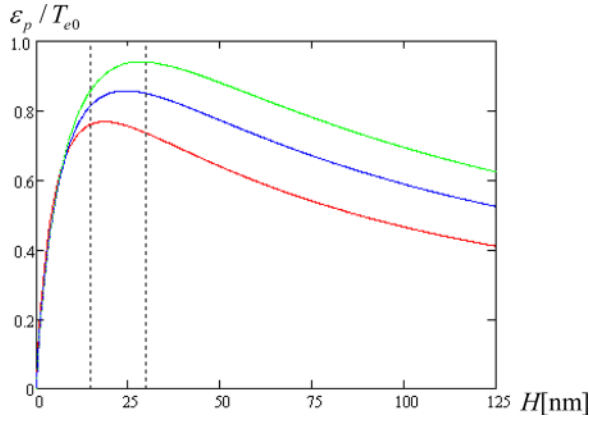


FIG. 6. The dependence of maximal normalized proton energy on cylinder length H (in nm) at different outer cylinder radius marked by different color $r_2 = 7.5, 15, 22.5$ nm, $\Delta r = 3$ nm, and $H_0 = 25$ nm. Vertical lines show the positions of $h = 2, 4$.

then: $2\pi Z n_{i0} r_1 (r_2 - r) \approx \pi n_{e0} (2r_{De})^2 = T_e / e^2$, $r_{De} \sim r_1$. To create n_{i0} of solid density the condition $r_{De} \sim r_1 \gg r_2 - r_1$ should be fulfilled as it is an applicability condition of (9). In this case, the electrons are partly removed (their density is much less compare than the ions in the walls), but they create a cloud located around the cylinder. The necessary estimated laser intensity to create such configuration requires a cylinder target with the thickness of the wall (20 nm) close to the optimal thickness of thin plane target (see review paper¹) and should has the similar characteristics of fast protons. The changing of the plane target on the cylindrical one has been done here to increase directionality and mono-chromaticity of proton beam at maximal energy. Data from Ref. 1 suggest that maximal proton energy greater than 100 MeV may be obtained at $I_L \geq 10^{21}$ W/cm² and $t_L \geq 30$ fs. From the model, approximately 4% of laser energy can be converted into the energy of accelerated 200 MeV protons containing in 20 nm C⁶H¹ shell at $I_L \approx 3 \times 10^{21}$ W/cm² and $t_L = 45$ fs. These conversion coefficients are characteristic for thin optimum targets.¹

The time of flight of proton with an energy of 100 MeV for a distance of 1000 nm is about 30 fs and comparable with the laser pulse duration. During this time period (30 fs), the thin (20 nm) carbon foil will move a few 10 nm under the laser ponderomotive pressure.¹ This model is still true because the cylinder maintains its shape; therefore, a narrow energetic and angular distribution will be produced. The optimal thickness of cylinder is similar to the foil target.¹ A cylinder of diameter $r_2 > r_{De}$ is useless because of wider proton angular distribution generated (see Appendixes). Usage of heavier cylinder material (for example, Au instead of C) decreases shape modification ($\sim Z/A$, where A —atomic mass), but to obtain proton energy of 100 MeV, smaller sizes are needed, $\Delta r = 5$ nm, $r_2 = 200$ nm, $H = 600$ nm at laser intensity $\sim 10^{21}$ W/cm².

MODELING OF ION ACCELERATION IN A TARGETS OF ONE ION SORT

Unlike a two ion sort target (with a heavy slow moving ions), it is necessary, in a target with one ion sort, to take

into consideration its motion in the course of acceleration. For these targets, a thin cylindrical shell approximation is inapplicable. During ion acceleration, a shell will expand until a thickness comparable with initial radius because the radial ion velocities inward and outward are comparable (see Fig. 3(a)). Shell expansion must be considered and thus, the solution given by Eq. (3) is not true, under these conditions. The description of cylindrical shell from one ion species is consolidated to find the ambipolar field and to define the temporal evolution of target borders from ion equations of motion under this field. The Poisson equation (Eq. (1)) for the dimensionless density of hot electrons is linearly connected with the potential, using the dimensionless variables it can be written as

$$2 \left(\frac{\partial^2}{\partial \xi^2} + \frac{1}{\xi} \frac{\partial}{\partial \xi} + \frac{\partial^2}{\partial \varsigma^2} \right) \eta_e = \eta_e - \eta_{i0}(\tau) \theta(\xi - \xi_1(\tau)) \times \theta(\xi_2(\tau) - \xi) \cdot \theta(h(\tau) - |\varsigma|),$$

$$\eta_{i0}(\tau) = \frac{n_{i0} (\xi_2(0)^2 - \xi_1(0)^2) h(0)}{n_{e0} (\xi_2(\tau)^2 - \xi_1(\tau)^2) h(\tau)}. \quad (10)$$

It is more convenient to use the dimensionless variables $\xi = r/r_{De}$, $\varsigma = z/r_{De}$ because in 2D adiabatic approximation $T_e/n_e = \text{const.}$ and $r_{De} = \text{const.}$ Time in Equation (10) plays a role of the parameter determining the current size of a cylindrical shell. The dependence of ion density $\eta_{i0}(\tau)$ on time is following the law of conservation of full cylinder charge: $4\pi \int_{\xi_1(\tau)}^{\xi_2(\tau)} \xi d\xi \int_0^{h(\tau)} d\varsigma \eta_i(\xi, \varsigma, \tau) = \text{const.}$ Equation (10) together with equations of motion of cylinder borders (below) creates the system of equations which describe the adiabatic expansion of a cylinder heated by a short laser pulse

$$\frac{\partial^2 \xi_{1,2}}{\partial \tau^2} = -2 \frac{m_e}{m_i} \frac{\partial \eta_e(\xi = \xi_{1,2}; \varsigma = 0)}{\partial \xi_{1,2}},$$

$$\frac{\partial^2 h}{\partial \tau^2} = -2 \frac{m_e}{m_i} \frac{\partial \eta_e(\xi = (\xi_1 + \xi_2)/2, \varsigma = h(\tau))}{\partial \xi}. \quad (11)$$

The solution of this system allows to define the dynamics of the accelerating field and dynamics of the hot electron density. Solving the equations of motion of test particles in the obtained potential will result in determining the energy and angular features of the distribution function of accelerated particles. The solution of the Poisson equation (Eq. (10)) can be written down in a general form through a Green function where triple integral is expressed through single integral from modified Bessel functions. Consideration of the limiting cases of the common solution gives a more convenient overall picture of dynamics. The above analysis and simulations show that ion acceleration is efficient with a cylinder height many times greater than the radius. In this case, radial dynamics of the cylinder poorly depends from axial one and can be considered separately for the infinite cylinder. The solution for the infinite cylinder (the infinite limits of integration on ξ) has the following form:

$$\eta_e(\xi) = \begin{cases} 2\sqrt{2}\eta_{i0}(\tau)(-\xi_1 I_1(\xi_1/\sqrt{2}) + \xi_2 I_1(\xi_2/\sqrt{2}))K_0(\xi/\sqrt{2}) & \xi \geq \xi_2 \\ 2\sqrt{2}\eta_{i0}(\tau)(\xi_1 K_1(\xi_1/\sqrt{2}) - \xi_2 K_1(\xi_2/\sqrt{2}))I_0(\xi/\sqrt{2}) & \xi \leq \xi_1, \end{cases} \quad (12)$$

where $\xi_{1,2}$ depends upon time τ . The termination of a laser pulse, in the absence of noticeable shift of ions, is considered as the starting point. The boundary conditions for defining the border between the ions accelerated inside and outside (potential at extreme position) have the form: $\partial\eta_e/\partial\xi^* = 0$, where $\xi^* \in [\xi_1; \xi_2]$: $\xi_1 I_1(\xi_1 \sqrt{\eta_0/2\rho^2}) K_1(\xi^* \sqrt{\eta_0/2\rho^2}) - \xi_2 K_1(\xi_2 \sqrt{\eta_0/2\rho^2}) I_1(\xi^* \sqrt{\eta_0/2\rho^2}) = 0$. Thus, there are $N = \pi(\xi_2^2 - \xi_1^2)$ ions in the cylinder shell (per length unit), from them: $N_1 = \pi(\xi^{*2} - \xi_1^2)$ go inside and $N_2 = \pi(\xi_2^2 - \xi^{*2})$ outside. In Eq. (12), the initial electron temperature and density are connected with the laser parameters. The equation of shell border motion has the form shown Eq. (11). The model expressed by Equations (11) and (12) will be compared via 2D and 3D simulations in the following section. In 2D scenario, Eqs. (12) and (11) will be used and thus the energy of a proton moving inside the cylinder and reaching at the center is

$$\varepsilon_p = \frac{m_i T_{eh}}{2m_e} \left(\frac{\partial \xi_1}{\partial \tau} \right)^2 \Big|_{\xi_1=0}. \quad (13)$$

In the case of 3D modeling, the equations of motion of test particles in the potential $\xi_{1,2}(\tau)$ (Eq. (12)) are solved to find the energy and angular features of the distribution function of accelerated particles.

2D simulations

The interaction of laser pulse lasting $t_L = 45$ fs of intensity 3×10^{19} W/cm² with spot size of $5 \mu\text{m}$ (a super Gaussian transversal profile) with hydrogen H^{+1} infinite cylinder target of density 6×10^{22} cm⁻³ located along an x-axis in the beginning is modelled using modified 2D PIC code.¹⁰ The thickness of the proton shell is considered to be $0.1 \mu\text{m}$ and the radius of shell $1.5 \mu\text{m}$. The p-polarized laser radiation propagates in the positive direction of z-axis (Fig. 7) and the cylinder axis was directed along the x-axis.

Fig. 7(a) shows the asymmetry of proton density distribution which is inconsistent to the axial symmetry of above analytical model. This asymmetry is due to the laser polarization and ponderomotive pressure. The phase diagram (Fig. 7(b)) has a special shape, which is linked to a large impulse of protons moving inside the shell ($y \sim z \approx 5 \mu\text{m}$) and similar protons from outward shell ($z \approx 2.5$ and $z \approx 7.5 \mu\text{m}$). In Fig. 7(b), the maximal impulse ($0.12 m_i c$) of a proton in the center of the cylinder ($z = 5 \mu\text{m}$) is visible, which corresponds to the energy about 5 MeV. Comparing this value with the results of the model equations (Eqs. (11)–(13)) shows the temperature of electrons to be around 2 MeV. The numerical solution of equations (Eqs. (11) and (12)) models the proton energy (Eq. (13)) with these parameters at 4 MeV. Thus, analytical expressions (Eqs. (11)–(13))

describe the radial collapse of the infinite cylindrical shell and effectively estimate the energy of protons.

Simulation of 3D case

The interaction of a laser pulse with the shell cylinder target is modelled using three dimensional PIC simulations with PICongPU code.⁸ The cylinder material is hydrogen with a density of 2×10^{22} cm⁻³. The shell radius is $1.5 \mu\text{m}$, thickness $0.1 \mu\text{m}$ and cylinder length is $5 \mu\text{m}$. The laser considered to be Gaussian in space and time with a beam diameter of $4 \mu\text{m}$, pulse duration $t_L = 45$ fs and pulse intensity of 3×10^{19} W/cm². A simulation box of dimension $5 \times 5 \times 8 \mu\text{m}^3$ corresponding to the grid size $384 \times 384 \times 384$ with cell size of 15 nm is used with a time step of 25 attoseconds. The boundary conditions are reflecting by considering the reflecting speed small in comparison to the speed of light. The p-polarized laser pulse (polarization of laser is along x-axis) interacts with the shell target along the y-axis in the XZ plane. The axis of cylinder is along the z-axis and starts at

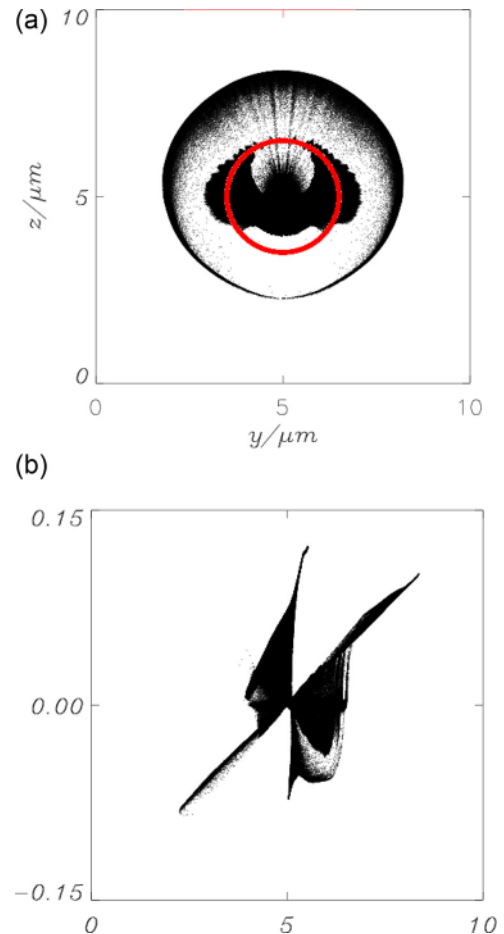


FIG. 7. Spatial distribution (a) and the $P_z z$ phase diagram (b) of proton density in a shell proton target with a radius of $1.5 \mu\text{m}$ at the time of 122 fs. The initial density distribution of protons is shown in red.

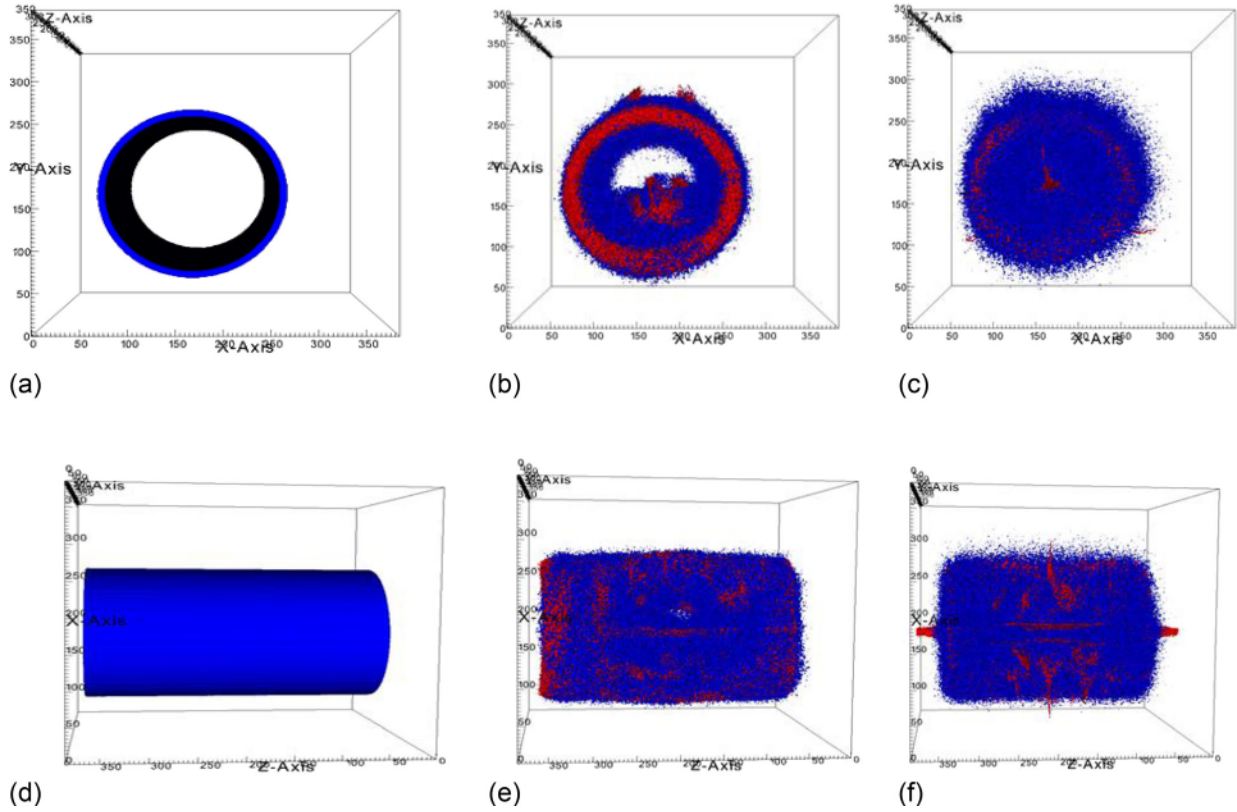


FIG. 8. Evolution of electron (blue) and ion (red) density distribution in hydrogen shell target: top view—at $t = 0$ (a), $t = 250$ fs (b), $t = 300$ fs (c); side view—at $t = 0$ (d), $t = 250$ fs (e), $t = 300$ fs (f). The x , y , and z -axis represent the number of cells where one cell size is 15 nm.

$z = 0.5 \mu\text{m}$ and terminates at $5.5 \mu\text{m}$. At $t = 0$, the density of ions in XY and XZ plane of shell target is shown in Figs. 8(a) and 8(d), respectively. As the laser pulse hits the shell target at 62.5 fs, a jet of hydrogen ions is generated in XY plane that collide with counter-propagating ions jet at the center of XY (Fig. 8(b)) (see also Ref. 7). The ions start to collapse at 150 fs after the laser hits the target. Figs. 8(b) and 8(c) show the ions in XY plane along the cylinder axis, as a consequence of the ion jets collapse and hence the accelerated ions through the cylinder axis. Just after collision, the ions jet propagates in z -direction in XZ plane in both the forward and backward directions (Fig. 8(f)). The ions momentum along the cylinder axis is due to the transient electric field inside the cylinder. As the laser hits the shell cylinder, it injects hot electrons which are confined over a Debye length on the cylinder's inner surface, generate a space charge field, which accelerate ions towards the axis of cylinder. The resulting radial electric field, due to plasma expansion, accelerates ions along the cylinder axis after its collapse from counter propagating ion jets.

Fig. 9 shows the energy spectrum of protons at $t = 300$ fs, where there is a narrow energy spread of protons at peak energy of 19.5 MeV.

The maximum proton cutoff energy exceeds 40 MeV at the time $t = 300$ fs; after this moment, the maximum proton energy decreases from this maximum cutoff value. The energy spectrum in all energy range looks like the quasi-thermal energy distribution with occurrence of a peak.

The analytical model of test particle motion (Eqs. (11) and (12)) enables the determination of the energy, and

Equation (7) produces the energy distribution function. The input data of the model are cylinder parameters, temperature and density of fast electrons, in particularly where $T_e \approx 2$ MeV at $I_L = 3 \times 10^{19} \text{ W/cm}^2$. From the simulations, r_{De} is found to be approximately $0.4 \mu\text{m}$. The motion of uniformly distributed along ζ test particles depends on the initial radial coordinate. The only protons located at $\xi_0 = 0.7\xi_1(0)$ and $0.3h < \zeta_0 < h$ have time to exit from the cylinder before the collapse and their distribution function is shown in Fig. 9 where the maximal value is normalized onto the simulation. The model correctly locates the position of the distribution function peak but the shape is slightly different because the simulated distribution function considers all protons.

The angle of incidence 45° for incident p-polarized laser on shell target along the y -axis in the XZ plane was also

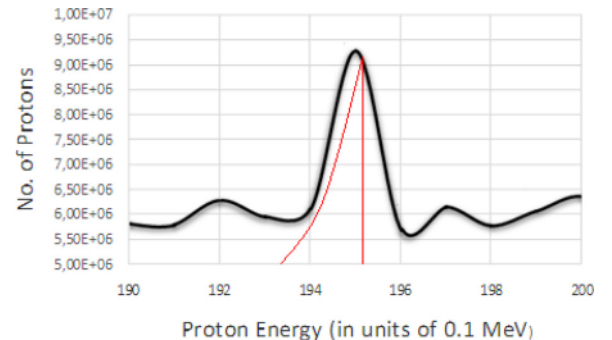


FIG. 9. The proton energy spectrum at $t = 300$ fs. Black line is the simulation result and red line is the result of the analytical model.

considered. With the oblique angle of incidence 45° , the maximum proton energy and number of protons accelerated along the z -axis of cylinder are decreased in comparison to the previous case because of decreasing intensity. The simulation results confirmed the proton acceleration along the z -axis of shell cylinder as a consequence of the collapse of proton beams on the z -axis, after explosively accelerated toward the z -axis.

The energy coupling efficiency is an important factor of the ion beam generation. It is defined as the ratio of the integrated kinetic energy of the bullet ions to all the electrons and ions. The latter one balances with the absorbed laser energy. In practice, the efficiency of the system can be enhanced if many nanotubes are in the focal region with optimal microscopic structure. Therefore, finally the

simulations of interactions of laser pulse have been performed with five cylinders. The density of hydrogen shell target is considered to be $6 \times 10^{22} \text{ cm}^{-3}$, shell radius $0.5 \mu\text{m}$, thickness $0.1 \mu\text{m}$, and shell length $3 \mu\text{m}$. The laser beam diameter is modelled as $2.0 \mu\text{m}$, pulse duration 45 fs, and pulse intensity $1.2 \times 10^{20} \text{ W/cm}^2$ and the laser beam is focused on the bottom on the central shell cylinder.

The beam diameter is deliberately larger than the individual shell diameter in order to accelerate ions from the entire surface of shell cylinders. Figure 10 shows the interaction of incident laser field with the hydrogen target of five shell cylinders followed by the laser field dynamics and subsequent electron and ion density distribution. The focusing of proton bunch starts at 200 fs and a maximum proton energy about 40 MeV is obtained which is higher from the

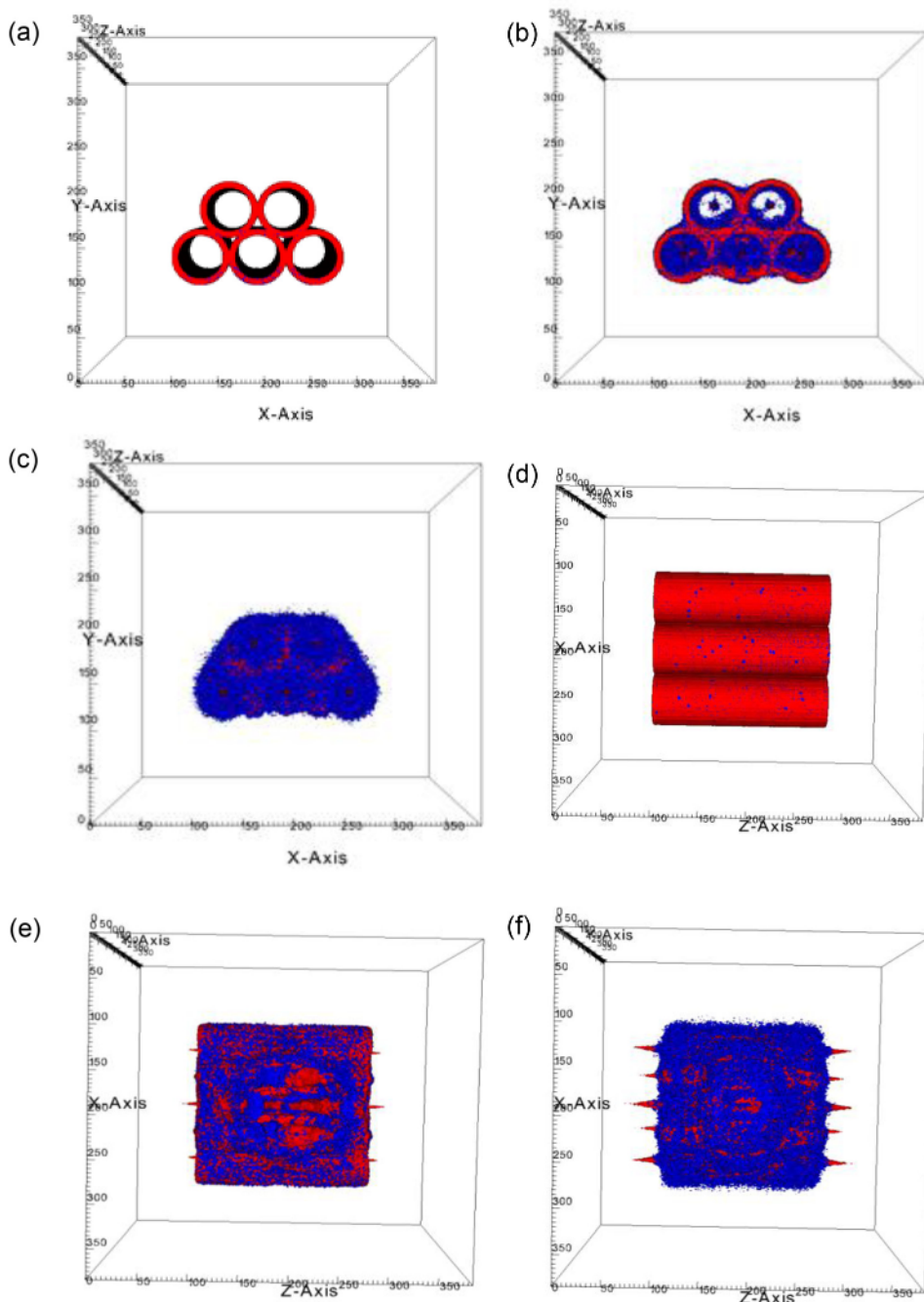


FIG. 10. Evolution of electron (blue) and ion (red) density distribution in an arrangement of five shell cylinder at different time moment: top view—at $t = 0$ (a), $t = 250$ fs (b), $t = 300$ fs (c); side view—at $t = 0$ (d), $t = 250$ fs (e), $t = 300$ fs (f). The x , y , and z -axis represent the number of cells where one cell size is 15 nm.

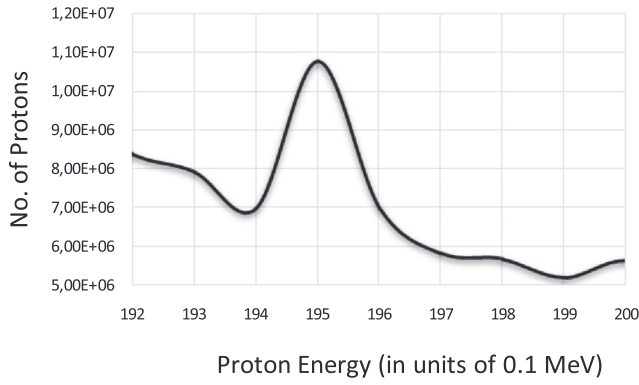


FIG. 11. The proton energy spectrum at $t=300$ fs. The maximum cutoff energy reaches around 40 MeV.

case of single shell cylinder. However, the proton energy peaked at roughly the same energy as before (Fig. 11).

CONCLUSION

In summary, we have proposed the ion acceleration scheme using target consisted from nano-shell cylinders that operate under irradiance of ultrashort, ultraintense laser pulses, to produce high-quality ion beams. Detailed three-dimensional particle simulations have demonstrated the generation of quasi-monoenergetic highly collimated 20-MeV proton beams at relativistic laser intensity.

The higher concentration of hot electrons within a shell target ensures higher proton energy compared to flat targets of the same size. The shell target is proposed to

have a higher density of hot electrons, filling the cylinder cavity for a substantial period. A lower cooling rate, due to this high concentration of electrons, is expected to contribute to the enhancement of the ambipolar field, and thus to the higher proton energy from the shell target. In a shell target, ions are accelerated both inward and outward from the shell. The inward acceleration leads to a collapse of the target and production of high density core. As a laser pulse hits a shell cylinder target, a narrow jet of energetic light ions is generated from heavy cylinder open boundaries.

APPENDIX A: ANALYTICAL MODELLING OF PROTON DEPARTURE ANGLE

When the Debye radius is less than a radius of the cylinder: $\rho \ll \sqrt{\eta_0}$, potential is described by Eq. (4) and the radial potential well is deep.

The type of heavy ion cylinder potential is given in Fig. 12(a). Here, the radial potential well is deep enough so there were radial oscillations of protons at the initial moment located near $z \sim 0$. The trajectory of such protons is given in Fig. 12(b) by the red line. The protons located closer to the end of the cylinder make a periodic motion as shown by the blue line in Fig. 12(b). The majority of protons thus manages to oscillate before departing from the cylinder and leaving with larger angles. The dependence of departure angle on the initial coordinate of a proton is given in Fig. 13(a). The derivative is getting close to zero at one (in module) angle and it leads (see (6)) to the existence of the peak at this angle on an angular distribution function, i.e., to a

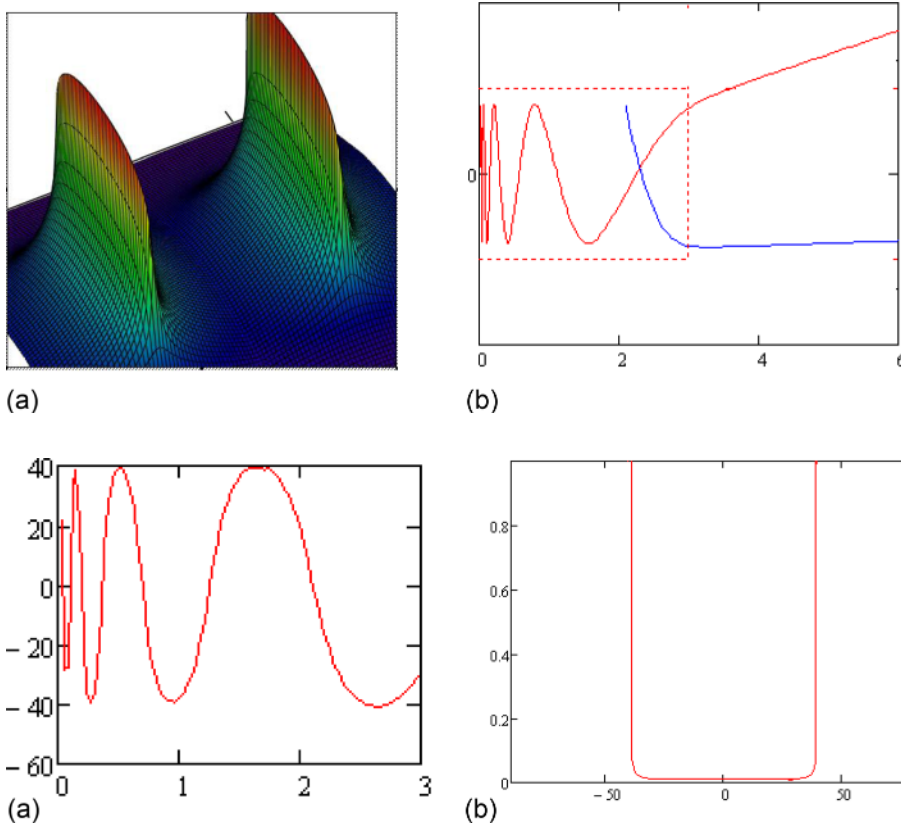


FIG. 12. (a) The potential of heavy ions (4). (b) Trajectories as function of initial provision of a proton in the cylinder. Parameters: $\sigma = 1$, $\xi_1 = 1$, and $h = 2$.

FIG. 13. (a) Departure angle as function of initial position of a proton in the cylinder at $\rho \ll 1$. (b) Dependence of proton distribution function on departure angle. Here $\sigma = 1$, $\xi_1 = 1$, $h = 2$.

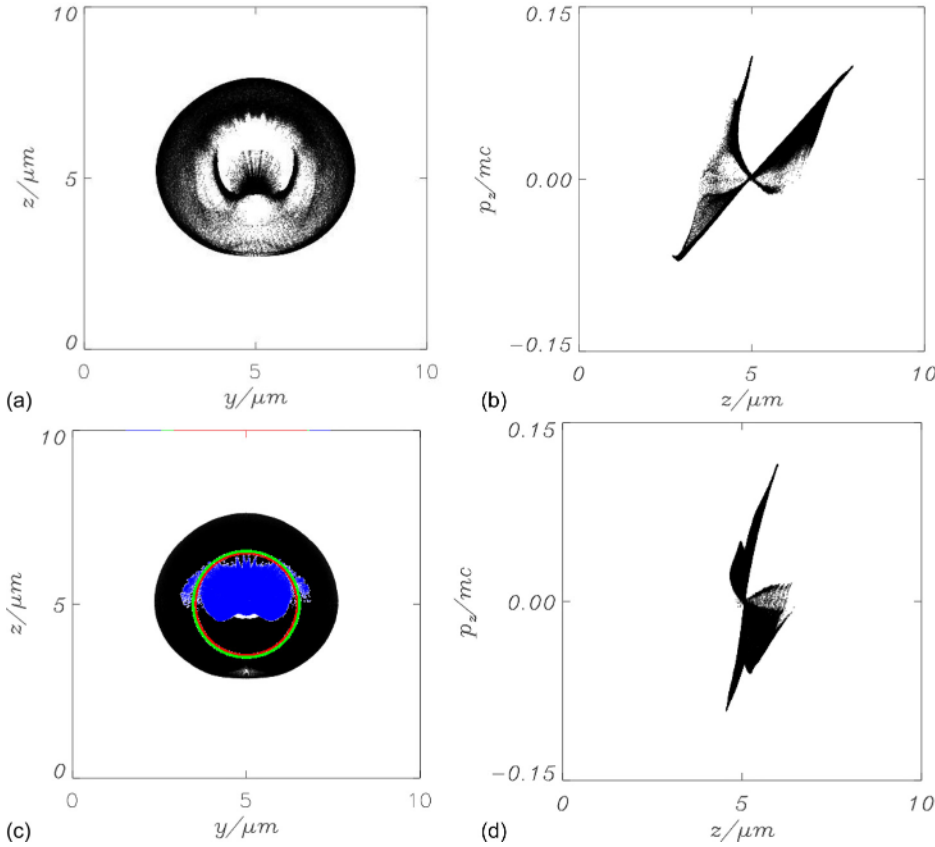


FIG. 14. (a) Proton density spatial distribution. (b) Proton phase diagram in homogeneous shell target. (c) Ion density spatial distribution. (d) Proton phase diagram in heterogeneous shell target.

departure of protons in the form of a cone. The dependence of proton distribution function on departure angle is given in Fig. 13(b).

Reducing the potential wall depth decreases the cone angle of proton angular distribution (as it was for the case $\rho \gg 1$). The energy distribution is not very sensitive to the hole depth and is defined by a potential distribution at cylinder edge. In a point of potential maximum ($z=0$) $E_z=0$ and according to Eq. (7), the high peak of proton distribution function is available at this point. In other range of energies (determined by dispersion of initial proton energies), the distribution function is terminating and its form weakly depends on ρ . Only the peak position is changing on energy scale, because for $\rho \gg 1$, $\rho \ll 1$ the potential is different at the point of proton start.

APPENDIX B: NUMERICAL MODELLING OF 2D SHELL COLLAPSE

Numerical modeling of the interaction of laser pulse (45 fs, intensity 3×10^{19} W/cm², spot size $5 \mu\text{m}$ —a super Gaussian transversal profile) with C^{+6} H^{+1} infinite in x-direction cylinder target of density 6×10^{22} cm⁻³ located along an axis x was performed using modified 2D PIC code.⁶ The initial radius of the shell was $1.5 \mu\text{m}$. In the case of a homogeneous target, the thickness of mixed carbon and hydrogen shell was 100 nm. In the case of heterogeneous target, the outer C-shell was of 100 nm and the inner proton shell thickness was 20 nm.

Acceleration of ions in a spherical shell leads to target “collapse”. Fig. 14 shows the density of protons at $t = 106$ fs. The initial position of the carbon shell is shown by the green line. For any heterogeneous target with a concentration of hydrogen on an internal surface (red cycle), protons are accelerated in 2 directions, inside and outside, forming two fronts. The proton “stream” which arises in a place of laser pulse interaction is clear visible in Fig. 14(a). The uniform filling of a target interior with protons happens at around 0.1 ps. For C^{+6} ions, there is a similar picture of driving however the process is slower and they reach the target center on times ~ 0.3 ps.

¹H. Daido, M. Nishiuchi, and A. S. Pirozhkov, *Rep. Prog. Phys.* **75**, 056401 (2012).

²S. Iijima, *Nature* **354**, 56 (1991).

³A. Andreev and K. Platonov, *Opt. Spectrosc.* **111**, 200 (2011).

⁴H. Xu, W. Yu, M. Y. Yu, A. Y. Wong, Z. M. Sheng, M. Murakami, and J. Zhang, *Appl. Phys. Lett.* **100**, 144101 (2012).

⁵M. Murakami and M. Tanaka, *Appl. Phys. Lett.* **102**, 163101 (2013).

⁶K. Nishihara, H. Amitani, M. Murakami, S. V. Bulanov, and T. Zh. Esirkepov, *Nucl. Instrum. Methods Phys. Res., Sect. A* **464**, 98 (2001).

⁷T. Toncian, M. Borghesi, J. Fuchs, E. d’Humières, P. Antici, P. Audebert, E. Brambrink, C. A. Cecchetti, A. Pipahl, L. Romagnani, and O. Willi, *Science* **312**, 410 (2006).

⁸H. Burau, R. Widera, W. Honig, G. Juckeland, A. Debus, T. Kluge, U. Schramm, T. E. Cowan, R. Sauerbrey, and M. Bussmann, *IEEE Trans. Plasma Sci.* **38**, 2831 (2010).

⁹T. Sokollik, T. Paasch-Colberg, K. Gorling, U. Eichmann, M. Schnürer, S. Steinke, P. V. Nickles, A. Andreev, and W. Sandner, *New J. Phys.* **12**, 113013 (2010).

¹⁰A. Kemp and H. Ruhl, *Phys. Plasmas* **12**, 033105 (2005).